

High-Throughput Analysis of Multispectral Images of Breast Cancer Tissue

Umesh Adiga, Ravikanth Malladi, Rodrigo Fernandez-Gonzalez, *Student Member, IEEE*, and Carlos Ortiz de Solorzano, *Member, IEEE*

Abstract—Statistical analysis of genetic changes within cell nuclei that are far from the primary tumor would help determine whether such changes have occurred prior to tumor invasion. To determine whether the gene amplification in cells is morphologically and/or genetically related to the primary tumor requires quantitative evaluation of a large number of cell nuclei from continuous meaningful structures such as milk-ducts, tumors, etc., located relatively far from the primary tumor. To address this issue, we have designed an integrated image analysis software system for high-throughput segmentation of nuclei. Filters such as Beltrami flow-based reaction-diffusion, directional diffusion, etc., were used to pre-process the images resulting in a better segmentation. The accurate shape of the segmented nucleus was recovered using an iterative “shrink-wrap” operation. The study of two cases of ductal carcinoma *in situ* in breast tissue supports the biological observation regarding the existence of a preferential intraductal invasion, and therefore a common origin, between the primary tumor and the gene amplification in the cell-nuclei lining the ductal structures in the breast.

Index Terms—Cell, coherence, diffusion, segmentation, tissue.

I. INTRODUCTION

THE quantitative study of large tissue blocks is essential in understanding the spread of genetic heterogeneity and the process of tumor invasion. For example, the ductal carcinoma *in situ* (DCIS) of the breast, a malignant, pre-invasive form of breast cancer, is characterized by an abnormal proliferation of cancer cells through ductal structures that are meant to carry milk. These abnormal cells can be detected by analyzing gene amplification/deletion in the cell-nucleus [1], [2]. Determining whether the gene amplification in intra-ductal tissue is related

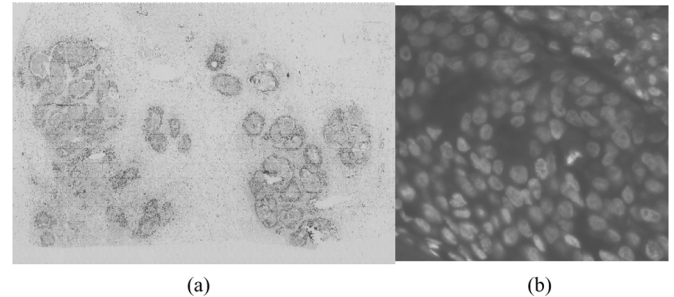


Fig. 1. (a) A 7.5×4.5 K image of a single slide obtained by montaging the 256×256 pixel images captured by the microscope from scanning of the complete tissue section. (b) A tiny part of the tissue image scaled to show distribution of the cell nuclei.

to the primary tumor requires analysis of cell nuclei that forms ducts and tumors in tissue blocks of the breast. An example image of a single tissue section of the DCIS specimen is shown in Fig. 1(a). In this image, consecutive images taken by the microscope were appropriately montaged to get a complete picture of the tissue section in one slide. The checker-board pattern that appears due to optical issues was removed by subtracting an image brightness pattern acquired over an empty area of the slide. A tissue block consists of a stack of several such slides where significant structures such as ducts and tumors are approximately registered. The spatial continuity of the structures in different sections is semi-automatically marked and the cell nuclei within these individual structures are analyzed for genetic heterogeneity. Fig. 1(b) shows a small part of a single channel of the multi-spectral tissue image. The algorithms for the reconstruction of three-dimensional (3-D) tissue blocks from two-dimensional (2-D) images, spatial delineation of tumors and other ductal structures, segmentation of nuclei, and quantifying the genetic makeup of cell nuclei in wide regions of interest together constitutes a high-throughput tissue image analysis system.

In spite of a number of techniques reported for tissue image analysis [3]–[5], segmentation of the cell nuclei in a compact tissue structure is still an open problem. The most recent survey of automatic segmentation of digital micrographs by Nattkemper [6] provides a review of several recently published articles on segmentation of micrographs. Though an exhaustive review is out of the scope of this paper, we briefly review some of the important papers in the field of segmentation of cells and tissues in 2-D micrographs. Gill *et al.* [7] in their review of image analysis and morphometry in breast cancer have concluded that the absence of any reliable nuclear segmentation technique is the main reason for the lack of automation in tissue

Manuscript received received April 19, 2005; revised August 31, 2005. This work was supported in part by the U.S. Department of Defense under Breast Cancer Research Grant DAMD17-00-1-0027 and Grant DAMD17-00-1-0336. The associate editor coordinating the review of this manuscript and approving it for publication was Dr. Robert F. Murphy.

U. Adiga is with the Lawrence Berkeley National Laboratory, University of California at Berkeley, Berkeley, CA 94720 USA (e-mail: upadiga@lbl.gov).

R. Malladi was with the Mathematics Department, Lawrence Berkeley National Laboratory, University of California at Berkeley, Berkeley, CA 94720 USA. He is now with the Imaging Technologies Laboratory, GE Global Research, John F. Welch Technology Center, Bangalore, India (e-mail: ravikanth.malladi@ge.com).

R. Fernandez-Gonzalez is with the University of California, Berkeley, and the University of California, San Francisco, Joint Graduate Group in Bioengineering and the Life Sciences Division, Lawrence Berkeley National Laboratory, University of California at Berkeley, Berkeley, CA 94720 USA (e-mail: rfgonzalez@lbl.gov).

C. Ortiz de Solorzano was with the Life Sciences Division, Lawrence Berkeley National Laboratory, University of California at Berkeley, Berkeley, CA 94720 USA. He is now with the Morphology and Imaging Group and Cancer Imaging Laboratory, Center for Applied Medical Research (CIMA), 31008 Pamplona, Spain (e-mail: codesolorzano@unav.es).

Digital Object Identifier 10.1109/TIP.2006.875205

image analysis. One of the early papers on the problem of segmenting cell nuclei in compact tissue images is that of Garbay [8]. They propose a region-growing technique that is constrained by shape and size similarities of cell nuclei. In dense tissue images of cancerous specimens, a more robust method is required. In high throughput tissue image analysis, the above method requires an automatic initial seed selection and becomes slow due to the requirement of continuous updating of similarity measures. The same issues limit the semi-automation method proposed by Wu and Barba [9], Sarti *et al.* [10], etc. Some of the thresholding based methods reported in the literature are Ganster *et al.* [11], Green *et al.* [12], Wu *et al.* [13]. Schnorrenberg *et al.* [14] proposed a soft-thresholding of a pre-processed breast cancer tissue image for cell counting. Thresholding methods are generally unreliable due to the non-uniform intensity distribution in fluorescent microscopy images. It is common knowledge that in many cases, multi-level thresholding fails to separate touching cells. Nedzeved *et al.* [15] and Schupp *et al.* [16] proposed morphological filters for cell-nuclei segmentation in tissue images. Generally, several morphological filters were used in various project specific combinations to achieve segmentation. When morphological filters are used, the shape of the segmented object tends to change in accordance with the shape of the structuring elements used for filtering. Wu *et al.* [17] propose a parametric model-fitting algorithm for cell segmentation. In this method, they assume objects are convex and hence a shape model can be used for segmentation. The result shown in [17] is on a tissue image with only two cell nuclei. The composition of the algorithm is also very complicated when overlapped structure are present in the image. Nattkemper *et al.* [18], Sjoström *et al.* [19] have suggested a neural network based segmentation method for high-throughput analysis of tissue sections. The method is based on training a neural-classifier over a large feature vector calculated from training-set and then use combination of basic morphological filtering and competitive layer model based neural classification to mark the cell contours. They have reported a success rate of 98% in classifying lymphocytes. Sjoström *et al.* [19] have argued that the neural network method as an alternative to NIH image software. The efficacy of both neural network based methods were not explored in detail e.g., when there is a change in the quality of the micrographs or the image acquisition settings or the change in tissue specimen. Yang and Parvin [20] have used a quadratic shape model whose parameters can be relaxed for the segmentation of nonstandard shapes. The reliability of this method was not proven on practical quality images obtained by non-confocal methods. Moreover, the preprocessing is tuned to particular type of noise found in specially stained confocal images making the method task-specific in nature. Zimmer *et al.* [21], Garrido and Blanca [22], Fok *et al.* [23], and Ray *et al.* [24] have used active models for the segmentation of cell nuclei. Considering the number of nuclei to be segmented, initializing the active contour models would pose a significant problem. Active models are prone to noise and other artifacts present in the tissue image.

This paper takes the approach of integrating several pre-processing filters to strengthen the edge or boundary features of cell nuclei for facilitating subsequent segmentation by a water-

shed based region-growing approach. Accuracy of the segmentation is improved by a novel post-processing operation called “shrink-wrapping”. Some encouraging results are shown.

II. MATERIAL AND METHODS

Large breast cancer tissue blocks were physically sectioned into 5- μm -thick sections. Alternate sections were stained with Hematoxylin and Eosin (H&E) and a combination of nuclear counter-stain (Texas RED), fluorescence in situ hybridization targeting gene Her2 (marked using Orange Cy3 dyes) and centromere specific chromosomal locations (stained using fluorescein isothiocyanate, FITC). Low magnification (2.5 X) images of the H&E stained tissue sections and fluorescent sections were first acquired and approximately registered with each other to mark the spatial connectivity of the ducts, tumors, etc. Regions of interest (ROI), such as ducts and tumors, were semi-automatically extracted in the H&E stained tissue images and virtually mapped onto their neighboring fluorescent-stained tissue images. The ROI in the fluorescent stained tissue specimens were reacquired at much higher resolution for cell-nuclei segmentation and quantitation of genetic variation.

The image acquisition and analysis software system is designed in three parts. The first part facilitates low-resolution image acquisition, semi-automatic marking of ROI and, the approximate registration of the images to form a spatially coherent structure of ducts, tumors, etc., [25]. The second part of the software performs the automatic and accurate segmentation of the cell-nuclei in large tissue images of fluorescent specimens. The final part of the software records genetic heterogeneity within the nuclei. In this paper, we describe the methodology used to complete the second and final part of the analysis. The control flow diagram of the analysis process is shown in Fig. 2.

A. Image Standardization

Standardization of the brightness properties of the micrographs reduces the need to retune filter parameters when there is a small change in the input image quality. Image standardization is done by the selective stretching of the histogram and is implemented as follows.

The histogram is smoothed to reduce noisy peaks. The “major peaks” of the histogram are marked by searching the histogram curve. A “peak” is defined as a point on the histogram curve that is higher than the neighboring points and “major peaks” are the peaks that are at least as tall as 1% of the height of the mode point peak. Let I_{\min} and I_{\max} be the lowest and the highest gray values that correspond to major peaks. For a unimodal histogram, I_{\min} and I_{\max} are the points where the histogram curve falls below 1% of the height of the mode point while traversing from mode point towards minimum and maximum gray-value bins, respectively. The contrast of the pixels in the image having gray values in the range I_{\min} -to- I_{\max} are stretched using the relation

$$I(x, y) = \frac{(2^N - 1)}{I_{\max} - I_{\min}} \cdot (I(x, y) - I_{\min}) \quad (1)$$

where $\min \leq I(x, y) \leq I_{\max}$

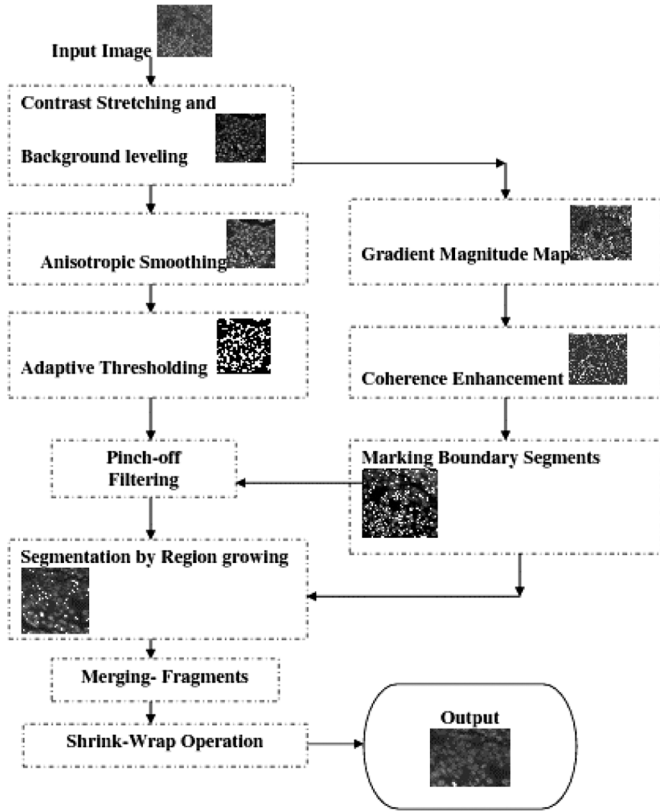


Fig. 2. Flow diagram of a generalized segmentation process for histo-pathological images.

Here, N is the number of bits used to represent a pixel in an image. This process modifies the intensity distribution in the image such that the data tends to have a similar intensity distribution and an approximately common mean brightness value.

The low-frequency brightness variation in the image caused by camera vignetting, etc., was reduced by background-leveling process. A background image was constructed by neighborhood averaging until objects disappear into the background. The background image was then subtracted from the contrast stretched image and the result was rescaled to occupy the complete gray-scale range.

B. Reaction-Diffusion Filtering

In histo-pathological images, the image pixel intensity gradient representing the boundary of the cell nucleus is the major feature facilitating accurate segmentation. When such features are too weak for complete boundary marking which is often the case in histological images, concavities in the overall object shape where more than one cell-nucleus touch or appear to overlap provide good indicators for a boundary search. A segmentation process, preceded by techniques aimed at enhancing these features would increase the efficiency of segmentation. This is accomplished first by denoising the tissue image using a reaction-diffusion filter and then by directional coherence enhancing filtering. Let us consider the image function $U_{t=0} = I(x, y)$ and $g = \nabla(U_{t=0})$ be the intensity gradient magnitude image where ∇ is the gradient operator and U_t indicates the image function at any given time “ t .” Malladi and Ravve [26]

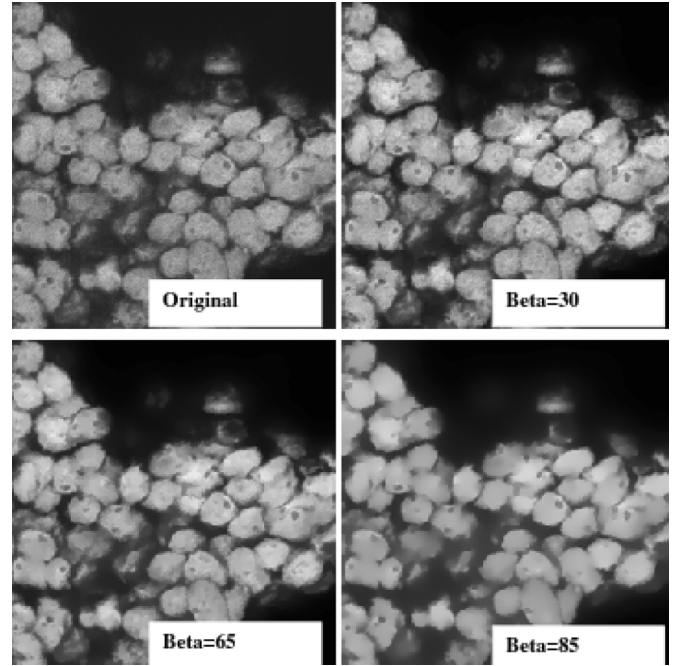


Fig. 3. Effect of reaction diffusion filtering at different “beta” values.

have proposed a following partial differential equation (PDE) as a reaction-diffusion type filter for image denoising

$$U_t = \cos^2 \beta \cdot \nabla \left(\frac{\nabla U_{t-1}}{g} \right) + \sin^2 \beta \cdot \frac{\nabla^2 U_{t-1}}{g}. \quad (2)$$

The first term on the right-hand side contributes to the reaction while the second term contributes to the nonlinear diffusion. The parameter β controls relative contribution of reaction and diffusion terms. To determine the value of β , we have applied the above reaction-diffusion filter on a seven representative data sets with the variable β in the range of 25° -to- 85° in steps of 5° increments. Fig. 3 shows the result of reaction-diffusion filtering for a fixed number of iterations with changing β values. At $\beta = 65^\circ$, all seven data-sets showed better segmentation result and hence $\beta = 65^\circ$ is considered as a default in the present application. A descriptive mathematical treatment and implementation details for filter represented by (2) can be seen in [26] and [27].

C. Boundary Coherence Enhancement

The second step of pre-processing is to enhance the boundary features of the nuclei. We have designed a directional coherence enhancement technique for this purpose. Coherence enhancement filtering has been implemented by different groups in the context of PDEs for image processing [27], [28]. We have implemented a real space directional coherence enhancement filtering as follows.

- 1) Calculate image intensity gradient map using image gradient operators.
- 2) At every pixel location in the gradient map, divide the local 3×3 neighborhood into four major directions i.e., horizontal, vertical and two diagonal directions. Calculate semi-Olympic average of the gradient magnitude in each

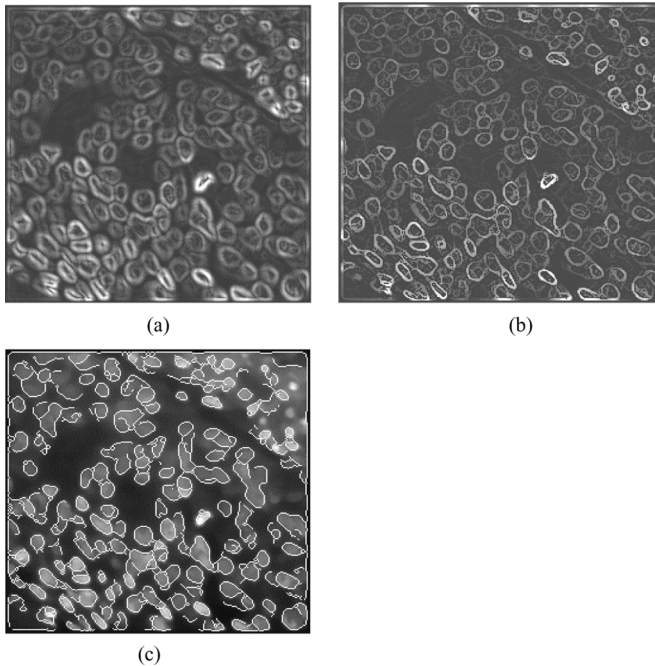


Fig. 4. Boundary coherence enhancement and synthesis. (a) Gradient magnitude image. (b) After directional enhancement. (c) Boundary synthesized from the gradient image.

direction within the 3×3 neighborhood. In semi-Olympic averaging, we discard the maximum value before calculating the average. This averaging process reduces the influence of noisy gradient peaks in the neighborhood and in an implicit way contributes inverse diffusion across the boundary.

- 3) Calculate local direction of the boundary as the direction in which the average gradient magnitude is maximum.
- 4) Replace the central pixel with the directional semi-Olympic average intensity value.

In addition to smoothing along the structure direction, the present implementation implicitly facilitates sharpening of the gradient peaks at the boundary. Use of semi-Olympic averaging reduces the probability of smoothing in an orthogonal direction within the neighborhood of the boundary. Fig. 4(a) shows the gradient magnitude in a small part of the tissue image. Fig. 4(b) shows the result of sharpening the gradient magnitude image by the above described process. The boundary segments of the cell-nuclei are synthesized from coherence enhanced image. All the pixels that are below the average gradient magnitude are discarded. A 3×3 pixel neighborhood at every pixel in the image is analyzed and only the three pixels with largest gradient magnitude in the neighborhood is retained as representing boundary segment. The synthesized boundary information is used as a supporting feature for segmentation of the cell-nuclei that are touching or overlapping one another. Fig. 4(c) shows the tissue image where the boundary segments of the objects synthesized from the coherence enhanced gradient map is superposed.

D. Binarization

There are several thresholding techniques, reported in the literature [29], which can be generally used as a direct method

for binarization. It is generally accepted that a single threshold for a large image may not be suitable for accurate binarization. The first issue that must be addressed is how to determine different regions in the image and the second issue is the calculation of corresponding threshold values for each region. Here we propose a simple technique that automatically determines the number of regions in the image and calculates regional thresholds.

We have implemented a multistep, adaptive region selection method to solve this problem. In the first step, we create different regions by amplitude thresholding at a fraction of the global threshold value $T_{\text{global}} = k \cdot \mu$ followed by component labeling. Here, k is determined such that the " T_{global} " is located near a shoulder point of the histogram that is close to the mean intensity " μ " of the image. The binary image is then labeled and each labeled component is considered as a region for which individual threshold values have to be determined.

The second step of binarization is based on the assumption that the individual regions have their brightness distributed in a smaller gray-scale range and most of the pixels in the individual regions belong to the objects. This second step consists of four substeps as follows.

- 1) The mode point of the smoothed histogram from individual regions is detected by scanning the histogram for the highest peak.
- 2) The gray values corresponding to the two shoulder points in the histogram are determined as the two points in the histogram located on either side of the mode point and, where the height of the peaks falls below 1% of the mode point height. This gray-scale range defines the threshold for the respective region.
- 3) Pixels whose gray-value is outside this range are converted to background, i.e., set to black in the binary image.
- 4) Pixels that correspond to the boundary segments synthesized from the coherence enhanced gradient map are converted to background pixels for further isolating the closely located binary structures.

The method is simple and effective in distinguishing different regions in the tissue image and setting a proper threshold based on the local region brightness distribution. Holes within the objects that appear due to intra cellular objects, etc., and that are darker than the rest of the object, are filled by analyzing the negative of the binary image. Tiny detectable objects in the negative image are considered as the holes in the positive image. Fig. 5 shows the result of multi-level thresholding on a small part of the tissue image. The binary image is then labeled and morphologically "opened" using a structuring element with an approximately circular effective kernel.

E. Segmentation of Nuclei Clusters

This stage of analysis determines the success of the methodology for the high-throughput analysis of cancer tissue images. A region-growing technique with automatic seed planting, whose growing abilities are constrained by the object boundary, shape, and the gray-scale features, is proposed for this purpose. This method closely follows the generalized watershed algorithm [30].

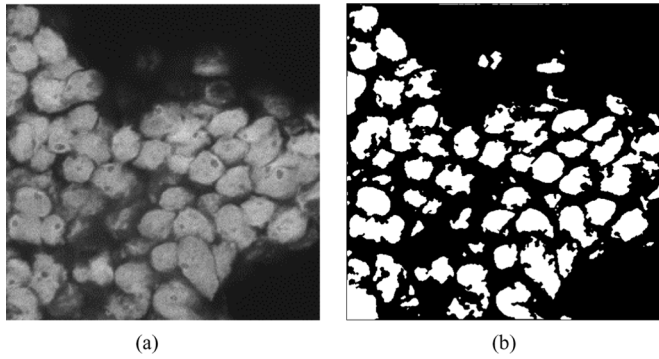


Fig. 5. Result of multistage region-based thresholding. (a) Image of dense tissue section. (b) After two-stage thresholding and hole-filling.

A distance map of the binary image is generated using Borgefor's distance-transforms [31]. This distance map provides a grey-scale representation of the binary tissue image where the local distance maxima represent the center of an object or the seed-points to start region growing. The grey-level of the objects in the distance map decreases from the seed-points towards the object boundary.

Let $\text{dist}(\cdot)$ represent the distance value of pixels in the distance map. List the distance values in the map in a descending order. Let, d_{\max} be the maximum distance in the distance map, d_{next} be the next maximum distance level and $d_{\min}(=0)$ be the minimum distance value in the distance map. The region growing in the distance map is described below.

- 1) The groups of pixels having maximum distance d_{\max} in the distance map are considered as initial set of seeds and are labeled using the connected-component labeling algorithm.
- 2) The region/seed growing is accomplished by merging the pixels having distance value d_{next} with the seed in its immediate neighborhood. Those groups of pixels with distance value d_{next} but not located in the immediate neighborhood of a seed are considered new seeds and are labeled accordingly. At the end of this step all the pixels with distance value d_{next} have a unique label attached to them showing that they belong to a seed region.
- 3) Recalculate d_{next} as the maximum distance value of the pixels in the distance map that are not labeled as seed regions.
- 4) If $d_{\text{next}} \geq d_{\min}$, then steps 2 and 3 are repeated.

Fig. 6 diagrammatically describes the region-growing process in a distance map. Two cell-nuclei of different sizes are connected together in such a way that binarization will not be able to segment them as shown in Fig. 6(a). Fig. 6(b) shows the distance map of the binary image shown in Fig. 6(a). At the start of the region growing, only "seed1" acts as a seed since only the pixels of "seed1" have distance value d_{\max} . After a few iterations of region growing, when the d_{next} value is same as the distance value of still unmarked "seed2," there will be two isolated groups of pixels with value d_{next} and ready to be merged with a seed. One such group is in the immediate neighborhood of "seed1." The other group has no seed in its neighborhood. This later group of pixels would be considered as

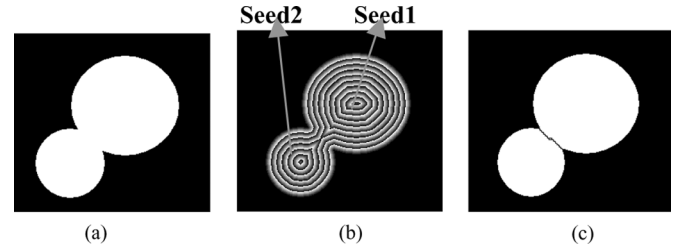


Fig. 6. Diagrammatic representation of region-growing concept over a distance map. (a) A binary image of a cluster of two objects. (b) The distance map of the cluster of two objects. (c) After region growing from the two seeds (local distance peak), the cluster of two objects is segmented.

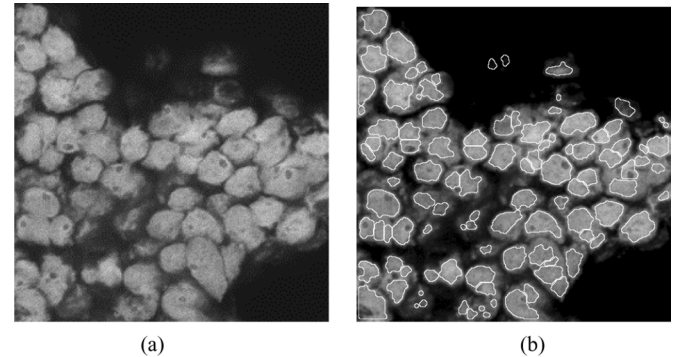


Fig. 7. Result of segmentation. (a) Dense tissue image. (b) Boundary of the isolated regions are overlaid on the original image. Inaccuracy in boundary marking can be clearly observed.

a new seed "seed2" and the region-growing process continues until all the object pixels are allotted a unique seed label. Fig. 7 shows the result of segmentation of tissue image by the above described process. Fig. 7(a) is the original gray-scale image while Fig. 7(b) shows overlaying of the boundary of isolated regions on the original image.

The noisy artifacts in the image and improper structural smoothing of the binary image might create noisy local maxima in the distance map that causes fragmentation of the cell-nuclei as shown in Fig. 7(b). It is necessary to recognize the fragments and merge them to an appropriate cell-nucleus. This is done in a few simple steps.

- 1) All the objects with relative size less than 0.5 are marked as fragments. The relative size of the object is defined as the ratio of the size of that object to the average size of objects in the image. The size of the object is the total number of pixels in the object.
- 2) The fragments are merged with a large object with which they share the boundary.
- 3) If the fragment is connected to more than one object, then it is merged with that object with which it shares larger common boundary.

It is possible that a single object is fragmented into many tiny segments and these segments are merged into different objects. Some of the tiny fragments that are not connected to any large objects and whose average grey level is very low are eliminated from the segmented image. The resulting image is structurally smoothed using a circular structuring element by a morphological "opening" operation. Fig. 8(b) shows the result of merging the fragments with connected larger objects.

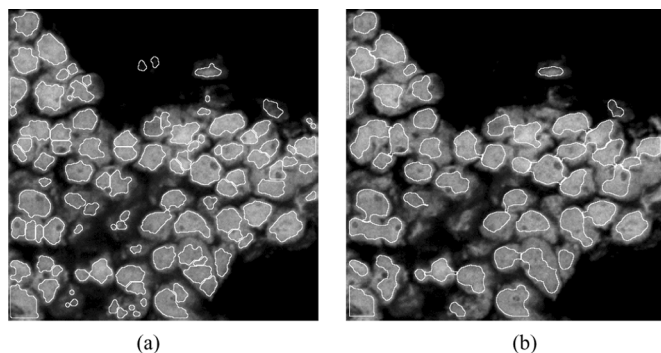


Fig. 8. Result of merging fragmented nuclei and eliminating isolated fragments. (a) Result of segmentation by region growing over a distance map is superposed on the original gray scale image. (b) Result after heuristically merging the fragments and structural smoothing by gray scale morphological closing.

If the objects can be generally categorized as convex shapes, shape-filters can be incorporated to identify fragments. Shape-based filters are effective in isolating non-nuclear artifacts or the cells whose shape change significantly due to malignancy.

F. Shrink Wrapping

The accuracy of segmentation obtained by sequential combination of filters depends on the accuracy of individual filter output. For example, the shape of the segmented objects is generally influenced by the shape of the structuring elements used for morphological smoothing, noise reduction, etc. Segmentation of clusters by region-growing using a distance-map relies on the presence of a concavity in the binary image where two or more objects touch one another. Thus the separation line obtained by the segmentation need not correspond to the pixel locations with high local gradient magnitude. Fig. 7(b) shows how inaccurate the segmented object shape can be when overlaid on the original gray-scale image.

To regain accurate shape of the objects, we have implemented an iterative process called “shrink-wrap” filtering. Here we consider the segmented objects as partial signatures of the cell-nuclei.

- 1) Label the objects in the segmented image.
- 2) The labeled objects are dilated into their immediate neighborhood under the constraint that the dilated objects do not touch one another.
- 3) The objects are shrunk along their boundary only if the gray-level of the boundary pixels is below the average gray-level of the dilated object. Object boundary shrinking is an iterative process. The object shrinking continues till there is no object boundary pixel whose gray-level is below the average gray-level of the dilated object.
- 4) Steps 2 and 3 are repeated until the difference between the size of the objects before and after an iteration of shrink-wrap operation, becomes zero.

Fig. 9 shows the result of shrink-wrapping for improving the accuracy of segmentation. Fig. 9(a) shows the boundary of the objects prior to dilate and shrink-wrap and Fig. 9(b) shows the boundary of the objects after shrink-wrapping.

Objects that are bloated beyond their actual boundary before the start of the shrink-wrap process, are simply shrunk back to their original shape and no major change in shape or size occurs

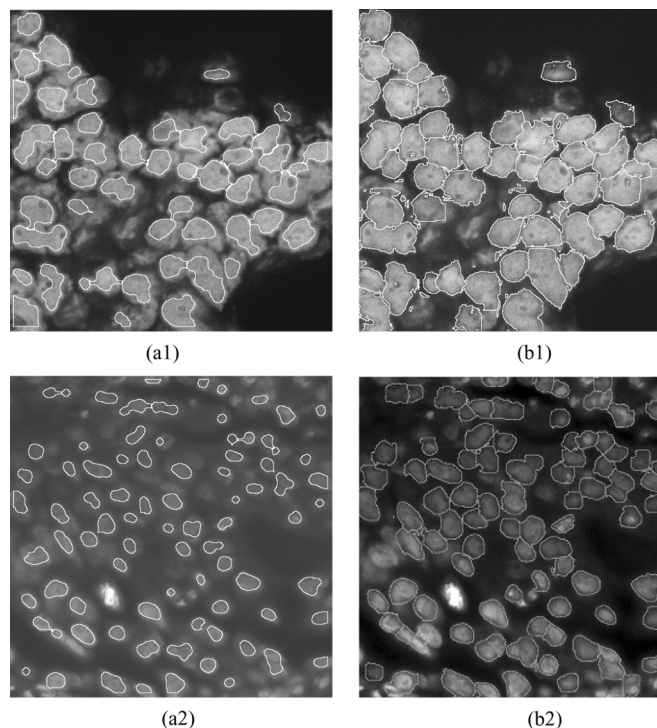


Fig. 9. Result of post-processing by shrink-wrapping. (a1) Dense tissue image after segmentation by region growing. (b1) After post-processing: the boundary contours of the segmented regions are over-laid on original image. (a2) Simpler sparse tissue image after segmentation by region growing. (b2) After post-processing: The boundary contours of the segmented regions are over-laid on original image.

in the subsequent iterations. The advantage of this shrink-wrap process is that the shrinking takes place based on the intensity characteristics of the individual cell nuclei. Thus, in malignant tissues individual nuclei that show different brightness features are not unduly influenced by the property of the pixels belonging to other cell nuclei.

III. ANALYSIS OF GENETIC HETEROGENEITY IN DCIS

By using fluorescence *in situ* hybridization (FISH), the genome amplification within the cell nuclei can be marked as fluorescent spots. Fig. 10 shows a FISH channel of a multi-spectral tissue image. Relatively bright-spots are considered as FISH signals. The tissue structures also make a ghost presence due to bleed-through from one spectral channel to another. Bleed-through is a common phenomenon in multispectral images where, the brightness of pixels at one spectral channel appears at the low intensity scale of other spectral channels and is considered noise. A healthy cell is expected to show two spots corresponding to the two normal copies a gene of interest. The malignancy or the tumor growth is generally highlighted by the amplification/deletion of the gene numbers, i.e., variation in the number of spots within the nucleus depicting the gene of interest. The level of magnification of the genome in cell-nuclei is considered as a way to determine genetic heterogeneity between different parts of the tumor or cancerous organ. For an accurate quantitative analysis, 3-D imaging by confocal microscope is essential [32], [33]. However, light scattering and hybridization efficiency limits the thickness of the sections

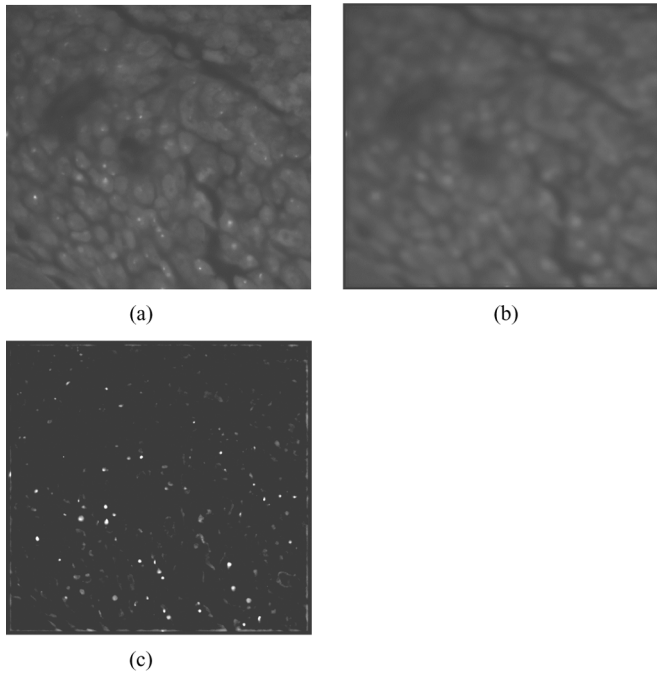


Fig. 10. Result of processing FISH signal channel. (a) Original image of the FISH signal channel (Her2 gene). The bright spots are the FISH signals and the rest is a bleed-through from the tissue image channel. (b) Reconstructed background image representing bleed-through. (c) After bleed-through reduction and rescaling.

that can be analyzed using confocal microscopy to less than $40\ \mu\text{m}$. This is very small compared the usual thickness of our samples (3–5 mm). This thickness is required to be able to preserve meaningful connected tissue structures such as ducts, etc., to study the DCIS of a breast cancer tissue block. Even if light penetration and sample preparation allowed staining and imaging of such thick blocks, the amount of data produced would be too large. By studying only the amplified genomes instead of deleted ones as a marker of cancerous cells, one can reduce the inaccuracy of the quantitative analysis due to 2-D slicing of the tissue block. We propose to distinguish cancerous from normal cells using the number of copies of the Her2 gene shown as bright spots in the FISH signal image [Fig. 10(a)]. The centromere FISH spots show no amplification in malignancy and are used as a control to study Her2 gene amplification. In summary, our argument favoring a standard 2-D fluorescent microscope stems from factors such as the amount of data to be analyzed, complexity of the data and the reduced necessity of multidimensional imaging due to the analysis of large number of cell nuclei.

To identify genetically aberrant cells one might count the number of FISH signals (fluorescent spots) present in the cell nuclei or integrate the fluorescence intensity in the area of the nucleus for the FISH signal channel. A simple algorithm for detecting the FISH signal spots is as follows.

- 1) Construct a background image of the FISH channel by inverse top-hat filtering. The difference between total intensity of the pixels in the rim of the top-hat and the kernel of the top-hat filter is calculated. If this difference is above a certain threshold, then the intensity of the pixels in the kernel is replaced by the average intensity of the pixels

of the rim of the top-hat filter. We have used a “ 7×7 ” top-hat filter with “ 3×3 ” kernel size located at the center. Fig. 10(b) shows the result of constructing background image of the FISH channel by inverse top-hat filtering.

- 2) Subtract the background image from the FISH image, convert all negative pixel values to zero and rescale the image. Fig. 10(c) shows the result of background subtraction and rescaling to enhance the FISH signal spots.
- 3) Threshold the FISH image at an appropriate gray level. The default threshold is the average brightness of the nonzero pixels.
- 4) Resolve the closely located FISH spots, if any, by fitting a FISH signal feature profile to local intensity peaks in the FISH spots [33]. A FISH signal feature profile consists of the size of an ideal FISH spot and the intensity distribution around the central peak, which is generally Gaussian.
- 5) Label and count the FISH spots in each cell-nucleus.

A similar study can also be done by calculating the integrated brightness of the pixels per cell-nucleus in the FISH channel and conducting a comparative analysis to determine genetic variation. The nonlinear brightness variation due to bleed-through from the other spectral channels decreases the efficiency of measuring genetic variation as an integral brightness of the FISH channel pixels within a cell-nucleus.

We have consistently observed gene amplification in the cells of milk-ducts, etc., even quite far from the tumors. The amplification of the number of FISH spots per cell-nuclei across the tissue block within a continuous structure such as ducts have reinforced the biological observation that the genetic heterogeneity exists far from the primary tumor prior to tumor invasion.

IV. RESULTS AND DISCUSSION

To evaluate the efficiency of the algorithm we used three tissue blocks taken from two different DCIS cases. Physical sectioning of the tissue block into several $5\text{-}\mu\text{m}$ -thick tissue sections resulted in an image stack of 5×5 K images for each of the 140 slides, with an average nuclei density of 20 000 nuclei/tissue-block. Our target was to achieve more than 85% of the cell-nuclei segmentation for large images that contain more than 2000 cell nuclei and to accomplish this task even when the quality of the image is relatively poor. The integrated method described in this paper has satisfied the target efficiency irrespective of the size of the image, and the number of objects to be segmented. As shown in the Fig. 10(b), even when the cell-nuclei are compactly arranged, the proposed method can clearly segment cell-nuclei and mark a boundary with good accuracy. To prove the general applicability of the methodology, we have tested the algorithms on 2-D images obtained from confocal microscopy are the cells were dense and compactly arranged. More than 98% of the cells are segmented correctly when the tissue images of the confocal image quality are used.

Table I shows the result of segmentation of cell-nuclei in a few representative slides for two cases of DCIS. In some cases, the false positives have gone beyond 10% of the segmented nuclei. A false positive is an object that has been segmented and recognized as a cell-nucleus by the algorithm while it is discarded as an artifact by an expert. Such false positives exist in some of

TABLE I

ANALYSIS OF EFFICIENCY OF IMAGE SEGMENTATION. THE TABLE LISTS A FEW RANDOMLY SELECTED TISSUE IMAGES, TOTAL NUMBER OF CELLS COUNTED MANUALLY IN THOSE TISSUE IMAGES, NUMBER OF CELL-NUCLEI SEGMENTED BY THE SOFTWARE, AND THE NUMBER OF FALSE POSITIVES IN THE SEGMENTATION RESULT

Case	Slide #	# of Nuclei (manual count)	# of Nuclei segmented by software (%ge correct seg.)	False Positives (%)
1.	1	5731	5538 (88%)	438(8%)
	2	4733	4333 (87%)	211(5%)
	3	4338	4691 (95%)	431(10%)
	4	3609	3655 (92%)	309(9%)
2	1	4064	4166 (94%)	327(8%)
	2	3171	3301 (87%)	523(16%)
	3	4008	3941 (89%)	372(10%)
	4	2089	2289 (93%)	328(15%)
	5	2007	2109 (93%)	230(11%)
	6	2061	2101 (93%)	183(9%)

the images due to the segmentation of brightness saturated cell nuclei and incompletely represented cell nuclei that occur at the border of the image. These are counted as cell nuclei by the software while the human expert has removed them from the nuclei category.

All the image analysis steps were completed using a fixed set of parameters, unchanged from experiment to experiment and case to case. This make us believe that the standardization of the intensity features of the tissue images followed by adaptive pre-processing steps prior to segmentation has successfully proved that the tuning parameters need not be changed every time new data is analyzed.

The importance of accuracy of delineating nuclear boundary depends on the application. In cases such as cell counting, it is not necessary to have an accurate boundary or shape etc., so long as one would count the same number of cell-nuclei and accurately recognize a counted nucleus. It is important to have accurate shape information for classification of cells of different tissues, to distinguish healthy cell-nuclei from malignant ones, to quantify genetic changes in the nuclei, etc. There are several instances where FISH signals are located very close to the nuclei boundary. If the boundary is not precisely drawn, then there is a chance that such a signal will be discounted as outside the nuclei or as belong to the neighboring nuclei that is closely located.

The accuracy of segmentation can be measured as a percentage of symmetric difference in the area of the cell-nuclei given by automatic segmentation and manual segmentation. If " A_1 " is the area of a cell nucleus segmented by an automatic method, i.e., set of all pixels in the nucleus segmented by automatic method and " A_2 " is the area of the same nucleus segmented manually then the percentage of symmetric difference is given by $(\{A_1 \cup A_2\} \setminus \{A_1 \cap A_2\}) / (\#A_2) \times 100$, where " \cup " is the set union operator, " \cap " is the set intersection operator, and " \setminus " is the set difference operator.

TABLE II

COMPARATIVE ANALYSIS OF CORRECTLY SEGMENTED CELL-NUCLEI BY THREE DIFFERENT SEGMENTATION METHODS IN SEVEN REPRESENTATIVE IMAGES. MULTILEVEL THRESHOLDING IS SIMILAR TO THE BINARIZATION DESCRIBED IN THIS PAPER. WATERSHED TECHNIQUE IS IMPLEMENTED AS DESCRIBED IN [30]

Specimen (slide) #	Integrated Approach (Proposed method)	Multi-level thresholding	Watershed algorithm
1	5100	3433	3831
2	4122	2172	2488
3	4260	3100	3781
4	3346	1731	2466
5	3839	2350	2743
6	2778	968	1371
7	3568	1179	2065

TABLE III

FISH SIGNAL ANALYSIS: SHOWS THE VARIATION IN FISH SIGNAL SPOTS/NUCLEUS (AS A STANDARD DEVIATION OF FISH SPOTS/NUCLEUS) IN CONTINUOUS SPATIAL STRUCTURES OF TWO DCIS CASES. EACH STRUCTURE IS AN ISOLATED REGION OF INTEREST IN 3-D. THOUGH THE NUMBER OF NUCLEI SEGMENTED FROM THESE STRUCTURES, ARE GENERALLY MORE, WE HAVE CONSIDERED ONLY THOSE NUCLEI SHOWING GENE AMPLIFICATION AND THE COUNT OF SUCH NUCLEI IS GIVEN IN COLUMN2

Case. #1	Number of Cells where gene- amplification is detected	Std. Dev. in number of FISH spots/nucleus Signal
Structure #1	1749	0.465
Structure #2	1931	0.658
Structure #3	1856	0.839
Structure #4	2101	0.925
Avg. Std. Dev. of FISH signal 0.721 spots/nucleus in case #1 =		
Case. #2		
Structure #1	1760	1.241
Structure #2	1720	1.02
Structure #3	931	1.13
Structure #4	2611	3.38
Structure #5	1176	1.307
Structure #6	1118	1.366
Avg. Std. Dev. of FISH signal 1.574 spots/nucleus in case #2 =		

One-hundred cell nuclei were randomly selected from different images and their boundaries manually delineated. The percentage symmetric difference in the area of each of the cell nuclei when segmented manually and automatically was calculated. We have found that such a percentage difference never exceeds 7%, which is an acceptable error limit. There is no generally accepted segmentation technique for delineating cell nuclei and hence it is difficult to compare the proposed methodology to other state-of-the-art techniques. Table II lists the number of correctly segmented nuclei in a few specimen images when multi-level thresholding and watershed algorithms, were applied. Based on the results in Table II, it can be argued that the proposed method performs much better compared to the other two methods.

Genetic heterogeneity as a function of the number of FISH signal spots/nucleus was calculated based on those cell-nuclei that show gene amplification. Table III shows the variation of

FISH spots/nucleus in cells from different structures of interest in two DCIS cases. The existence of genetic heterogeneity in the cells of the tissue structures that are relatively far from the primary tumor confirms the earlier observation by Holland *et al.* [1] and Lagois *et al.* [2]. The high standard deviation of the spot count need not indicate higher genetic heterogeneity. It generally indicates that the amplification of the number of copies of the gene of interest is not uniform among the cells of the tissue.

Most of the functions in the software are written in IDL. C was used for low-level processing of images. Software is tested on a 512-Mb RAM, 1GHz speed, Win2000 PC. For an image of approximately 5×5 K size, it takes approximately 15 min to complete the segmentation and analysis of fluorescent signatures.

ACKNOWLEDGMENT

The authors would like to thank the referees for their constructive comments, which greatly helped in bringing this manuscript to the current shape. The efforts by Dr. R. J. Hall of Lawrence Berkeley National Laboratory for improving the English and the readability of the manuscript is acknowledged with thanks.

REFERENCES

- [1] R. Holland, J. L. Connolly, R. Gelman, M. Mravunac, J. H. Hendriks, A. L. Verbeek, S. J. Schnitt, B. Silver, J. Boyages, and J. R. Harris, "The presence of an extensive intraductal component following a limited excision correlates with prominent residual disease in the remainder of the breast," *J. Clin. Oncol.*, vol. 8, pp. 113–118, 1990.
- [2] M. D. Lagios, P. R. Westdahl, F. R. Margolin, and M. R. Rose, "Ductal carcinoma in situ," *Cancer*, vol. 40, pp. 1309–1314, 1982.
- [3] K. Preston Jr. and P. H. Bartels, "Automated image processing for cell nuclei and tissue," in *Progress in Medical Imaging*. Berlin, Germany: Springer Verlag, 1988, pp. 1–121, (Newhouse eds.).
- [4] H. Nazeran, F. Rice, W. Moran, and J. Skinner, "Biomedical image processing in pathology: A review," *Australas. Phys. Eng. Sci. Med.*, vol. 18, no. 1, pp. 26–38, 1995.
- [5] S. H. Ong, X. C. Jin, Jayasooriah, and R. Sinniah, "Image analysis of tissue sections," *Comput. Biol. Med.*, vol. 26, no. 3, pp. 269–279, 1996.
- [6] T. W. Nattkemper, "Automatic segmentation of digital micrographs: A survey," presented at the 11th World Congr. Medical Informatics, 2004.
- [7] J. Gil, H. Wu, and B. Y. Wang, "Image analysis and morphometry in the diagnosis of breast cancer," *Microsc. Res. Tech.*, vol. 59, no. 2, pp. 109–18, 2002.
- [8] C. Garbay, "Image structure representation and processing: A discussion of some segmentation methods in cytology," *IEEE Trans. Pattern Anal. Mach. Intell.*, vol. PAMI-8, pp. 140–146, 1986.
- [9] H. S. Wu and J. Barba, "An efficient semi-automatic algorithm for cell contour extraction," *J. Microscopy*, vol. 179, pp. 270–276, 1995.
- [10] A. Sarti, C. Solorzano, S. Lockett, and R. Malladi, "A geometric model for 3-D confocal image analysis," *IEEE Trans. Biomed. Eng.*, vol. 47, no. 12, pp. 1600–1609, Dec. 2000.
- [11] H. Ganster, A. Pinz, R. Rohrer, E. Wilding, M. Binder, and H. Kittler, "Automated melanoma recognition," *IEEE Trans. Med. Imag.*, vol. 20, no. 3, pp. 233–239, Mar. 2001.
- [12] A. Green, N. Martin, J. Pfitzner, M. O'Rourke, and N. Knight, "Computer image analysis in the diagnosis of melanoma," *J. Amer. Acad. Dermatol.*, vol. 31, pp. 958–964, 1994.
- [13] H. Wu, J. Barba, and J. Gil, "Iterative thresholding for segmentation of cells from noisy images," *J. Microscopy*, vol. 197, pp. 296–304, 2000.
- [14] F. Schnorrenberg, C. S. Pattichis, K. C. Kyriacou, and C. N. Schizas, "Computer aided detection of breast cancer nuclei," *IEEE Trans. Inf. Technol. Biomed.*, vol. 1, no. 2, pp. 128–140, Mar. 1997.
- [15] A. Nedzved, S. Ablameyko, and I. Pitas, "Morphological segmentation of histology cell images," presented at the Int. Conf. Pattern Recognition, Barcelona, Spain, 2000.
- [16] S. Schupp, A. Elmoataz, P. Herlin, and D. Bloyet, "Mathematical morphologic segmentation dedicated to quantitative immunohistochemistry," *Anal. Quant. Cytol. Histol.*, vol. 23, no. 4, pp. 257–67, 2001.
- [17] H. S. Wu, J. Barba, and J. Gil, "A parametric fitting algorithm for segmentation of cell images," *IEEE Trans. Biomed. Eng.*, vol. 45, no. 3, pp. 400–407, Mar. 1998.
- [18] T. W. Nattkemper, H. Wersing, H. Ritter, and W. Schubert, "A neural network architecture for automatic segmentation of fluorescence micrographs," *Neurocomputing*, vol. 48, no. 4, pp. 357–367, 2002.
- [19] P. J. Sjöström, B. R. Frydel, and L. U. Wahlberg, "Artificial neural network aided image analysis system for cell counting," *Cytometry*, vol. 36, no. 1, pp. 18–26, 1999.
- [20] Q. Yang and B. Parvin, "Harmonic cut and regularized centroid transform for localization of subcellular structures," *IEEE Trans. Biomed. Eng.*, vol. 50, no. 4, pp. 469–75, 2003.
- [21] C. Zimmer, E. Labruyere, V. Meas Yedid, N. Guillen, and J. C. Olivo-Marin, "Segmentation and tracking of migrating cells in videomicroscopy with parametric active contours: A tool for cell-based drug testing," *IEEE Trans. Med. Imag.*, vol. 21, no. 10, pp. 1212–21, Oct. 2002.
- [22] A. Garrido and N. de la Blanca, "Applying deformable templates for cell image segmentation," *Pattern Recognit.*, vol. 33, pp. 821–832, 2000.
- [23] Y. L. Fak, J. C. K. Chan, and R. T. Chin, "Automated analysis of nerve cell Images using active contour models," *IEEE Trans. Med. Imag.*, vol. 15, no. 3, pp. 353–368, Jun. 1996.
- [24] N. Ray, S. T. Acton, and K. Ley, "Tracking leukocytes in vivo with shape and size constrained active contours," *IEEE Trans. Med. Imag.*, vol. 21, no. 10, pp. 1222–1235, Oct. 2002.
- [25] R. Fernandez-Gonzalez, A. Jones, E. Garcia-Rodriguez, P. Y. Chen, A. Idica, S. J. Lockett, M. H. Barcellos-Hoff, and C. Ortiz-de-Solorzano, "A system for combined three-dimensional morphological and molecular analysis of thick tissue specimens," *Microscopy Res. Tech.*, vol. 59, no. 6, pp. 522–530, 2002.
- [26] R. Malladi and I. Ravve, "FasT difference schemes for edge enhancing beltrami flow," in *Proc. Comput. Vis. Conf.*, 2002, vol. LNCS 2350, pp. 343–357.
- [27] N. Sochen, R. Kimmel, and R. Malladi, "A general framework for low level vision," in *IEEE Trans. Image Process.*, Mar. 1998, vol. 7, no. 3, pp. 310–318.
- [28] J. Weickert, Scale-space properties of non-linear diffusion filtering with a diffusion tensor Lab. Technomath., Univ. Kaiserslautern, Kaiserslautern, Germany, 1994, Rep. No. 110.
- [29] P. K. Sahoo, S. Soltani, A. K. C. Wong, and Y. C. Chen, "A survey of thresholding techniques," in *Comput. Vis. Graph. Image Process.*, 1988, vol. 41, pp. 233–260.
- [30] P. S. Umesh, Adiga, and B. B. Chaudhuri, "An efficient method based on watershed and rule based merging for segmentation of 3-D histopathological images," *J. Pattern Recognit.*, vol. 34/7, pp. 1449–1458, 2001.
- [31] G. Borgefors, "On digital distance transforms in three dimensions," in *Comput. Vis. Graph. Image Process.*, 1996, vol. 64, pp. 368–376.
- [32] K. Rodenacker, M. Aubele, P. Hutzler, and P. S. U. Adiga, "Groping for quantitative 3D image analysis: An approach to quantitative evaluation of fluorescence in situ hybridization in thick tissue sections of prostate carcinoma," *J. Anal. Cell. Pathol.*, vol. 15, pp. 19–29, 1997.
- [33] P. S. U. Adiga, S. J. L. Knight, and B. B. Chaudhuri, "Characterization and automatic counting of FISH signals in 3-D tissue images," *J. Image Anal. Stereol.*, vol. 20, no. 1, pp. 41–52, 2001.



Umesh Adiga received the B.S. degree in electronics and communication engineering and the M.S. degree in electronics engineering from the University of Mysore, Mysore, India, the M.S. degree in computer science from Oxford University, Oxford, U.K., and the Ph.D. degree from the Indian Statistical Institute, Calcutta, India, in 1999.

He is a Scientist with the Physical Biosciences Division of Lawrence Berkeley National Laboratory, University of California, Berkeley. Prior to joining Lawrence Berkeley National Laboratory, he was a Postdoctoral Associate at the University of Arizona, Tucson, and Rensselaer Polytechnic Institute, Troy, NY. From 1999 to 2001, he was a Postdoctoral Scientist at the Wellcome Trust Centre for Human Genetics, Oxford University. From 1997 to 1998, he was a Visiting Scientist at the GSF Institute for Health and Environmental Sciences, Munich, Germany. His research interests include systems design for the quantitative analysis of micro to subnano resolution biomedical image data collected using optical, confocal, and electron microscopes.



Ravikanth Malladi received the B.E. degree in electrical engineering and the M.Sc. degree in physics from the Birla Institute of Technology and Sciences, Pilani, India, in 1988. He also received the M.S. and Ph.D. degrees from the Department of Computer Science and Engineering, University of Florida, Gainesville, in 1994. He underwent postdoctoral training at the Center for Pure and Applied Mathematics, University of California at Berkeley, Berkeley, CA, in 1994.

He joined GE Global Research in April 2004 as Manager for Imaging Technologies, Bangalore, India. He spent a decade at Lawrence Berkeley National Laboratory, University of California, Berkeley, working on developing schemes, algorithms, and code base for a large variety of image analysis applications. The specific applications range from medical, biomedical, cell, and nuclei imagery, seismic, and electron microscope imagery (cryo-EM). He has delivered over 55 invited talks, and has over 50 published papers in journals, book chapters, and conference proceedings on the topics of image processing, segmentation, representation, shape modeling and recognition, fast numerical schemes, and applied mathematics. His work has over 1275 citations in scientific literature.



Rodrigo Fernandez-Gonzalez (S'03) was born in Madrid, Spain, in 1978. He received the B.S. degree in computer engineering from the Universidad Autonoma de Madrid in 2000. He is currently pursuing the Ph.D. degree in bioengineering from the University of California, Berkeley, and the University of California, San Francisco.

Mr. Fernandez-Gonzalez is a student member of the American Association for Cancer Research, the International Society for Stem Cell Research, and the American Society for Cell Biology.



Carlos Ortiz de Solorzano (M'98) was born in Leon, Spain, in 1967. He received the B.Eng. and Ph.D. degrees in telecommunication engineering from the Universidad Politécnica de Madrid, Madrid, Spain, in 1992 and 1996, respectively.

From January 1997 to January 2000, he was a Postdoctoral Fellow at the Lawrence Berkeley National Laboratory (LBNL), Berkeley, CA. Later, he was a Scientist (2000–2002) and then a Staff Scientist and Principal Investigator (2002–2004) at LBNL's Bioimaging Group (Life Sciences Division). He is currently a Staff Scientist in the Oncology Division and Head of the Morphology and Imaging Laboratory of the Center for Applied Medical Research (CIMA) of the University of Navarre, Pamplona, Spain. His research interests include the fields of quantitative fluorescence microscopy and image analysis, with applications to studying the molecular mechanisms of normal tissue development and cancer. He has authored over 20 papers in a wide range of peer-reviewed journals.